ACS OMEGA

Open Access

http://pubs.acs.org/journal/acsodf

Article

3-Thiophenemalonic Acid Additive Enhanced Performance in Perovskite Solar Cells

Samuel Abicho, Bekele Hailegnaw, Felix Mayr, Munise Cobet, Cigdem Yumusak, Teshome Abute Lelisho, Teketel Yohannes, Martin Kaltenbrunner, Niyazi Serdar Sariciftci, Markus Clark Scharber, and Getachew Adam Workneh*

Cite This: *ACS Omega* 2024, 9, 2674−2686

Read Online

ACCESS | Metrics & More | Article Recommendations | Supporting Information

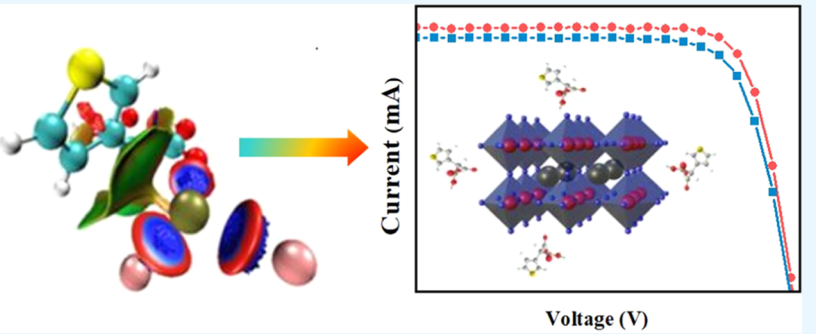

ABSTRACT: The development of ambient-air-processable organic−inorganic halide perovskite solar cells (OIHPSCs) is a challenge necessary for the transfer of laboratory-scale technology to large-scale and low-cost manufacturing of such devices. Different approaches like additives, antisolvents, composition engineering, and different deposition techniques have been employed to improve the morphology of the perovskite films. Additives that can form Lewis acid−base adducts are known to minimize extrinsic impacts that trigger defects in ambient air. In this work, we used the 3-thiophenemalonic acid (3-TMA) additive, which possesses thiol and carboxyl functional groups, to convert PbI_2, $PbCl_2$, and CH_3NH_3I to $CH_3NH_3PbI_3$ completely. This strategy is effective in regulating the kinetics of crystallization and improving the crystallinity of the light-absorbing layer under high relative humidity (RH) conditions (30−50%). As a result, the 3-TMA additive increases the yield of the power conversion efficiency (PCE) from 14.9 to 16.5% and its stability under the maximum power point. Finally, we found that the results of this work are highly relevant and provide additional inputs to the ongoing research progress related to additive engineering as one of the efficient strategies to reduce parasitic recombination and enhance the stability of inverted OIHPSCs in ambient environment processing.

1. INTRODUCTION

The unprecedented increase in power conversion efficiency (PCE) of organic−inorganic halide perovskite solar cells (OIHPSCs) from 3.9% in 2009[1] to 26.1% in 2023[2] is a great motivation for researchers as well as achievement in photovoltaic science and technology. Even though OIHPSCs exhibit many exciting optoelectronic features,[3,4] their instability toward extrinsic and intrinsic stresses[5] is profoundly hindering their scalability and commercialization. For example, large grain boundaries, pinholes, and residuals are instigating deep and shallow defects at the surface and/or interfaces, which induce degradation of the OIHPSCs.[6,7] Octahedral tilting, rotations, and deformations of corner-sharing PbI_6^{2-} octahedra are also suggested for lowering the performance of the OIHPSCs.[8−10] On the other hand, the oxidatively doped Spiro-OMeTAD layer, which is the most common hole transporting material in a standard planar OIHPSC structure, induces the leakage of air and moisture through it toward the photoactive layer.[11] Consequently, the overall performance of the OIHPSCs is abated because of the recombination of charge carriers at the surface and/or across interfaces.

To improve both the PCE and stability of the OIHPSCs, researchers are extensively exploring several approaches to reduce high trap density states in the OIHP polycrystalline thin films. In this regard, compositional engineering, incorporation of additives, interface, and surface passivation of the light absorber layer, careful selection of charge transport layers, solvent engineering, and use of proper electrode layers have been investigated extensively to minimize the barrier toward

Received: September 30, 2023
Revised: December 10, 2023
Accepted: December 22, 2023
Published: January 4, 2024

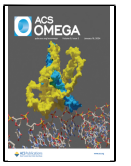

commercialization of OIHPSCs.[12−19] Structural engineering of a three-dimensional/two-dimensional (3D/2D) mixed perovskite structure has also been investigated to get stable and reproducible OIHPSCs.[20,21] In addition to this, the role of deposition techniques on whole performance has also been studied as one of the mechanisms to fabricate stable organic−inorganic halide perovskite (OIHP) devices.[22]

PbI_2 impurities can be formed by an incomplete conversion of the precursor materials to $CH_3NH_3PbI_3$ in dimethylformamide (DMF), which is ascribed to the so-called fast crystallization.[23] In this case, a nonhomogeneous photon absorber layer with pinholes and numerous grain boundaries is formed. As a result, nonradiative recombination can occur due to the defective surface. To improve the crystallization of the perovskite thin films, researchers have been working on a Lewis acid−base adduct approach, which involves the effective coordination of under-coordinated Pb^{2+} or I^- with additives that can donate or accept lone pair electrons.[24−26] This approach is mainly based on retarding the crystallization of PbI_2, which improves the crystallization of OIHP. Research results show that a uniform and smooth morphology of the OIHP thin films can be obtained by incorporating some appropriate additives.[27−29] Moreover, larger grain or fewer grain boundaries have been found to reduce the number of deep-trap states, which cause charge recombination on the surface of the OIHP thin films. The formation of ionic, covalent, or noncovalent bonds between ions or atoms in OIHP and additives/or passivators plays a vital role in suppressing the dissociation of OIHP films due to physical and chemical stresses.[30,31] In this regard, adding small organic molecules or organic salts as an additive to the OIHP solution has been employed as an effective and efficient strategy to augment the PCE and/or stability of devices in ambient air.

In this work, we introduced 3-thiophenemalonic acid (3-TMA) as an additive to the precursor solution of $CH_3NH_3PbI_3$ to enable facile crystallization in an ambient environment. The molecule possesses a thiol and two carboxyl functional groups. The binding of carboxyl functional groups with under-coordinated Pb^{2+} or I^- was disclosed from the results of Fourier transform infrared spectroscopy (FTIR) and X-ray photoelectron spectroscopy (XPS) measurements. Consequently, the results of surface morphology measurements indicated that a smooth surface with an improved average grain size was achieved for an optimized concentration of 0.30% (w/w). X-ray diffraction (XRD) shows that the characteristic diffraction peak intensity of the additive-containing devices is increased, which is ascribed to the improved crystallinity of the films. In addition to this, the extracted results ensure that PbI_2 is completely converted to $CH_3NH_3PbI_3$. Results from intensity-modulated photovoltage spectroscopy (IMVS) also indicate that the incorporation of the 3-TMA additive reduces the formation of the nonradiative recombination across a surface and/or interface of the photoactive films. Moreover, the additive-containing OIHPSCs showed improved photovoltaic performance and stability compared to devices without additives.

2. EXPERIMENTAL DETAILS

2.1. Materials. Indium tin oxide (ITO)-coated glass substrates (15 Ω cm^{-2}), lead iodide (PbI_2, Sigma-Aldrich, 99%), lead dichloride ($PbCl_2$, Alfa Aesar, 99.9%), [6,6]-phenyl-C_{61}-butryic methyl ester (PCBM, Solenne BV), 3-thiophenemalonic acid (TCI America, 98%), aluminum (Al), poly(3,4-ethylenedioxythiophene) polystyrenesulfonate ((PEDOT:PSS), Clevios PH1000), Zonyl FS-300 fluorosurfactant (40% in H_2O, Fluka), dimethylformamide (DMF, anhydrous, Sigma-Aldrich), dimethyl sulfoxide (DMSO, Anal. R. VWR chemicals, 99.5%), chlorobenzene (C_6H_5Cl, 99.8%, Sigma-Aldrich), chloroform (Anal. R. VWR chemicals), acetone (VWR Chemicals), isopropanol (VWR Chemicals), acetylacetone (AA, Sigma-Aldrich ≥99%), and Helmanex detergent (Hellma Analytics) were purchased from the commercial chemical suppliers and used as received. In addition, methylamine (33 wt %, in absolute ethanol, Sigma-Aldrich), hydroiodic acid (HI (aq), 57 wt %, Sigma-Aldrich), diethyl ether (VWR Chemicals), and ethanol (absolute, MERCK) were used to synthesize and purify methylammonium iodide (MAI) according to the literature.[32] TiO_x sol−gel was synthesized based on the procedure reported by Park et al.[33]

2.2. Preparation of the Perovskite Solution. $MAPbI_3$ solution was prepared by mixing a 1:1:4 mol ratio of PbI_2, $PbCl_2$, and MAI, respectively.[34] Then, different concentrations of 3-TMA in % (w/w) (0.15, 0.30, and 0.45) were added as the solid additives to the above mixture for optimization. Finally, the mixture of the perovskite precursors was dissolved in anhydrous DMF, which contains 10.0 vol % acetylacetone (AA) as the solvent additive, and was stirred overnight at about 45 °C.[16] Finally, the solution was filtered using a 0.45 μm polytetrafluoroethylene (PTFE) filter.

2.3. Device Fabrication. ITO-coated glass substrates were cleaned by using Hellmanex detergent solution, deionized water, acetone, and isopropanol (IPA) for about 20 min of each step in an ultrasonicator. Then, the cleaned substrates were dried under nitrogen (N_2) gas stream before starting the spin-coating process. A PEDOT:PSS (Clevious PH1000) solution was prepared by adding 7% of dimethyl sulfoxide (DMSO) and 0.7% Zonyl FS-300 fluorosurfactant and it was mixed well in order to enhance the conductivity.[35] The PEDOT:PSS (Clevious PH1000) solution was spin-coated as a hole transport layer (HTL) at 1250 and 2000 rpm for 45 s and annealed at 120 °C for 15 min. It was washed by spin-coating IPA (400 μL) at 2000 rpm for 2 s and 4000 rpm for 10 s and annealed again for 15 min at 120 °C. After cooling the PEDOT:PSS films to room temperature, the filtered solution of the perovskite ($MAPbI_3$) was spin-coated at 1250 rpm for 17 s and 2000 rpm for 5 s. After 1 min delay, the coated substrate was then transferred to a hot plate for annealing at 110 °C for 30 min. Then, 20 mg/mL PCBM solution in chlorobenzene and chloroform (1:1 vol ratio) was spin-coated on the absorber layer as an electron transport layer (ETL) at 1250 rpm for 16 s and 2000 rpm for 15 s. Here, it should be noted that all solutions (i.e., hole transport, perovskite, and electron transport layer solutions) were filtered with their corresponding filters before they had been deposited. Henceforth, TiO_x sol−gel was spin-coated on the top of the ETL at 5000 rpm for 30 s and annealed at 107 °C for 7 min. The whole device processing was performed in the ambient environment, and finally, the inverted perovskite solar device configuration: (ITO/PEDOT:PSS/$MAPbI_3$/PCBM/TiO_x/Al) was completed by thermal evaporation of 110 nm aluminum metal as a back electrode.

2.4. Characterization. The surface morphology of the films was characterized by using Bruker Innova atomic force microscopy (AFM) and scanning electron microscopy (Jeol SEM). The thickness of different layers was measured by a profilometer (Bruker Dektak.XT). X-ray diffraction (XRD)

https://doi.org/10.1021/acsomega.3c07592
ACS Omega 2024, 9, 2674−2686

patterns were measured by a Materials Research diffractometer, which is suitable for the structural characterization of the thin films under ambient conditions. It has a horizontal ω-2θ goniometer (320 mm radius) in a four-circle geometry and works with a ceramic X-ray tube with a Kα anode (λ = 1.540 Å). This diffractometer is equipped with different incident and diffracted optics, which can be interchanged depending on the application required (i.e., a parabolic mirror, a hybrid monochromator, a Ge (440) four-crystal monochromator, a parallel plate collimator, and a polycapillary lens). A PIXcel detector, which is a fast X-ray detector on Medipix2 technology with a 256 × 256 pixels array, was used. The characteristic photocurrent density−photovoltage (J−V) response of the solar cells with 0.15 cm^2 active cell area was measured by using a Keithley-2400-LV source meter. A LOT-QD solar simulator with a 1000 W xenon lamp providing an AM1.5 global spectrum was used for irradiation. The intensity of the solar simulator was calibrated by a silicon reference diode. This technique was also used to measure the hole-only device dark current density (J_D) to get the space-charge-limited current (SCLC) curves.

The external quantum efficiency (EQE) was measured by using an optical setup consisting of a lock-in amplifier (SR830, Stanford Research Systems) and a Jaissle 1002 potentiostat functioning as a preamplifier. Devices were illuminated with light from the xenon lamp passing through a monochromator (Oriel Cornerstone). A filter wheel holding long-pass filters and a mechanical chopper were mounted between the xenon lamp and the monochromator. Chopping frequencies in the range of 10−200 Hz were chosen. A silicon diode (Hamamatsu S2281) was used to determine the light intensity delivered by the setup at each wavelength.

Absorbance, transmittance, and reflectance of $MAPbI_3$ thin films with and without the 3-TMA additive were recorded with an ultraviolet−visible−near-infrared (UV−vis−NIR) spectrometer (PerkinElmer Lambda 1050). Tungsten and deuterium lamps were used as the light source to provide a wide wavelength range from 190 to 3100 nm.

An Osssila contact angle goniometer (L2004A1, Netherlands) was used to carry out the contact angle measurements of the HOIP films at room temperature using 18 MΩ ultrapure water.

Fourier transform infrared spectroscopy (FTIR) spectra were collected by an FTIR spectrometer (Bruker Vertex 80, equipped with a Bruker platinum attenuated total reflectance (ATR) accessory). XPS measurements were performed on a Theta Probe XPS system (Thermo Fisher). The system used a monochromated Al−Kα X-ray source with an energy of 1486.6 eV and a spot diameter on the sample surface of 400 μm. For high-resolution scans, a hemispherical analyzer was set to a pass energy of 20 eV at an energy step size of 0.05 eV. The system used a dual flood gun, which provided electrons and Ar^+ ions with low kinetic energy for charge compensation on the sample. Data acquisition and evaluation were performed via Avantage software (Thermo Fisher). For background correction of high-resolution XPS spectra, the smart background correction was used, which is based on a Shirley background, modified by the constraint that the background values cannot be at a higher intensity than the measured data. To correct charging, the binding energies of all spectra were referenced to the values of the Pb $4f_{7/2}$ binding energy of Pb(0) artifacts at 136.5 eV.[36]

Photoluminescence spectra of various devices were measured by using a Shamrock SR-303i monochromator and an Andor iDus Si-CCD detector. Samples were excited at 488 nm with a 5 mW power using a COHERENT OBIS 488−150 LS laser. A set of long-pass filters was used to avoid any distortion of the recorded spectra by laser light.

Intensity-modulated photovoltage spectroscopy (IMVS) measurements were executed under V_{oc} conditions under illumination with 10% light-modulated amplitude. IMVS measurement setups were proceeded as follows. Primarily, the OIHPSCs with and without additives were fronted to a light-emitting diode (LED). The parameters were set to measure the perturbed V_{oc}, which is DC voltage with 10% light intensity perturbation in the frequency range from 1 MHz to 50 mHz by using PhotoEchem software. Then, the values of LED light intensity were set by the program to vary the intensity by controlling the current applied to the LED source. Finally, the software generated an intensity calibration curve by using its NIST-calibrated reference photodiode and controlled the LED intensity directly via a LED driver (Thorlabs DC2100). To check whether the solar cell was properly connected and operated, the J−V characteristics were measured before the IMVS measurements.

2.5. Theoretical Calculations. Quantum chemical calculations were carried out using the M06-2X density functional[37] as implemented in Gaussian09 software.[38] The Los Alamos National Laboratory 2-Double-Zeta (LANL2DZ) basis set was used for lead and iodine[39] and the standard basis set 6-31+G(d,p) was used for other atoms. The noncovalent interaction (NCI) analysis was performed using the software called a multifunction wavefunction analyzer (Multiwfn).[40] Furthermore, visualization of the noncovalent interactions was displayed by the VMD program.[41]

3. RESULTS AND DISCUSSION

3-TMA, which is incorporated as a solid additive in the $MAPbI_3$ perovskite solution (Figure 1a), was employed to

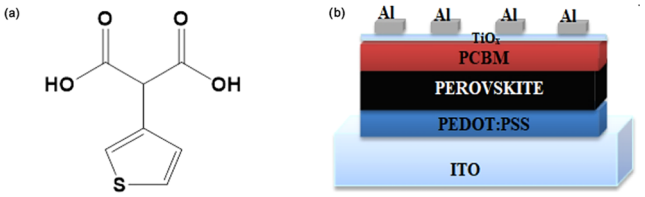

Figure 1. (a) Chemical structure of 3-thiophenemalonic acid and,(b) the p-i-n configuration of $MAPbI_3$ PSCs.

fabricate perovskite solar cells with the p-i-n architecture (Figure 1b). The compound contains the thiophene and carboxylic functional groups, which act as Lewis bases due to their lone pair electrons on oxygen and sulfur atoms. The presence of lone pairs of electrons on the compound provides the possibility to form either noncovalent or covalent interactions with lead ions (Pb^{2+}) or iodide ions (I^-) or hydrogen atoms in the ammonium cation.[42] Consequently, it is believed that chemical interactions, resulting from Lewis acids and bases,[43] could induce nucleation and control the kinetics of crystallization.[44,45] Thus, they can lower the degree of nonradiative recombination conception in a material.[46,47]

3.1. Chemical Interactions. *3.1.1. Computational Findings.* A computational calculation using M06-2X density

https://doi.org/10.1021/acsomega.3c07592
ACS Omega 2024, 9, 2674−2686

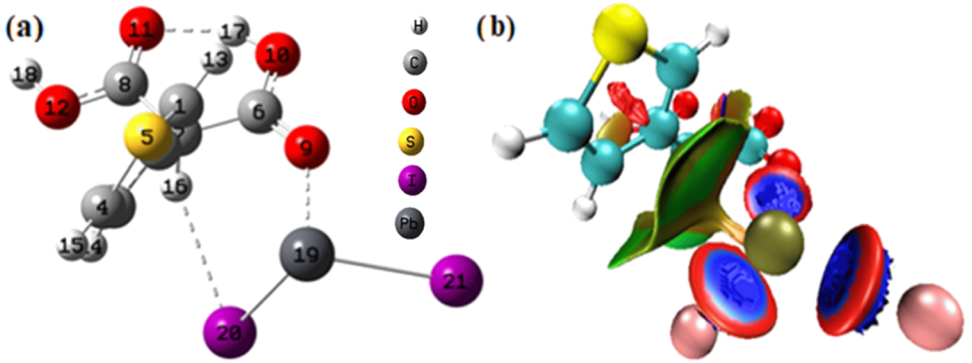

Figure 2. (a) Schematics of the most stable structure of the 3-TMA and PbI_2 and (b) isosurface map for NCI of the 3-TMA and PbI_2 complex, which are obtained using the M06-2X density functional.

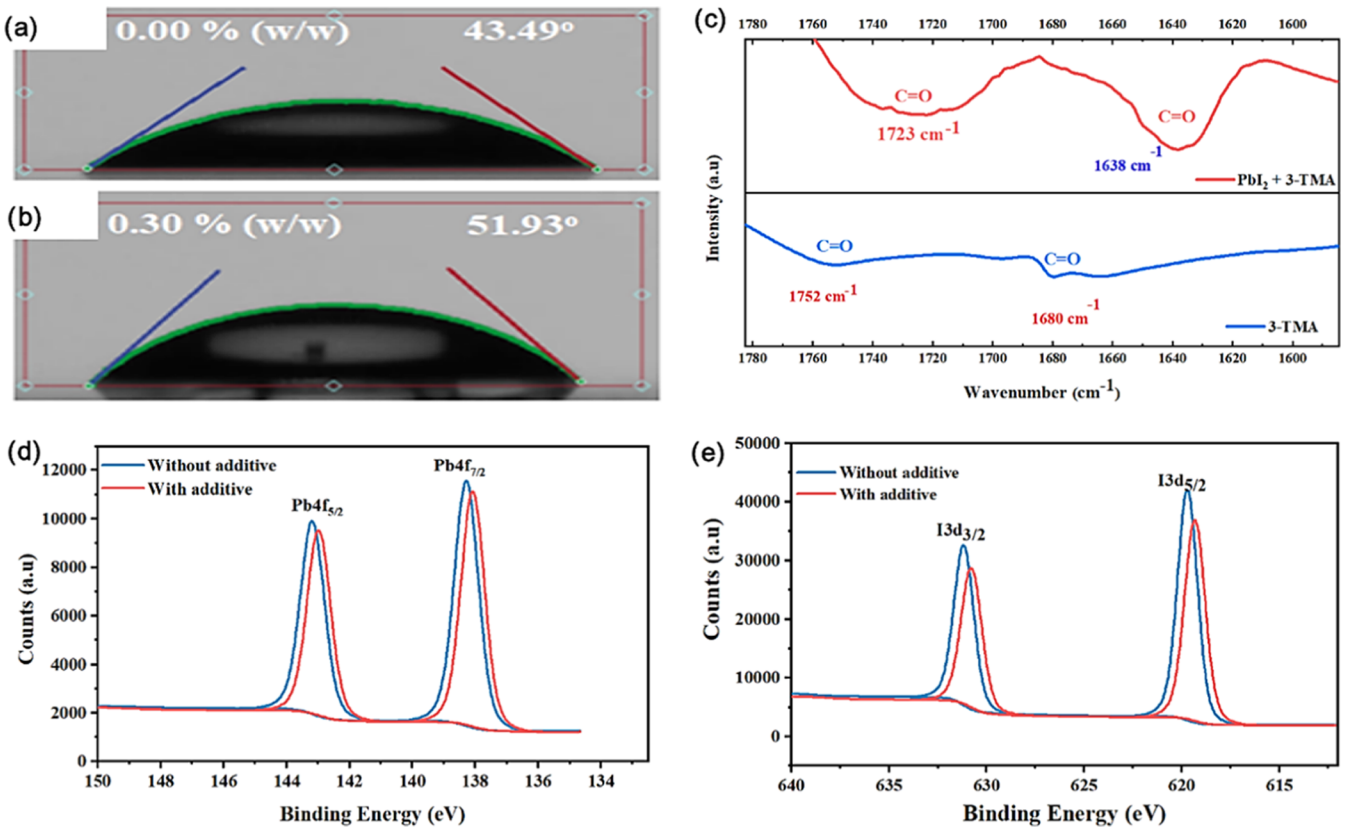

Figure 3. Contact angle of $MAPbI_3$ films (a) without and (b) with additives and (c) FTIR spectra of 3-TMA and PbI_2 thin films. XPS spectra indicate the characteristic core-level fitted peaks of (d) Pb 4f and (e) I 3d of films with and without additives.

functional theory (DFT) was applied to gain detailed insight into the possible interaction between PbI_2 and 3-TMA in the perovskite precursor. After generating the input structures of PbI_2 and 3-TMA, the most stable structure (Table S1) was used to carry out the noncovalent interaction (NCI) analysis (Figure 2a). Theoretical information, which visualizes the presence of NCI between nuclei of atoms, provides a better explanation for the existence of attractive van der Waals and repulsive forces.[48] These forces are indicated using an isosurface map of interaction region indicator (IRI), which are assigned by blue, light blue, green, light green, and red colors to show the type of NCI between atoms.[49,50] Accordingly, the presence of a blue disk (Figure 2b) between O9 (red) and Pb19 (gold) in the 3D isosurface map of the NCI plot ensures that the interaction is attractive. Besides, the presence of green isosurface between H16 (white color) and I20 (dawn pink color) reveals the existence of van der Waals interactions in the same figure.

Moreover, the energy density parameters are indicated in (Table S2) to provide possible clues for the nature of the interactions between atoms. In the aforementioned table, the Laplacian of the electron density ($\nabla^2\rho$), which is used to identify bond critical points (BCP), describes the strength of NCI between two nuclei of atoms.[51,52] Accordingly, the calculated positive $\nabla^2\rho$ values along the O9−Pb19, H16−I20 and π−Pb19 BCPs reflect the presence of NCI between atoms.[52] Further, the π electron density of the highest occupied molecular orbital (HOMO) level is indicated in Figure S1. It shows the possible van der Waals forces between the π system of 3-TMA and Pb^{2+}. In addition, the NCI

https://doi.org/10.1021/acsomega.3c07592
ACS Omega 2024, 9, 2674−2686

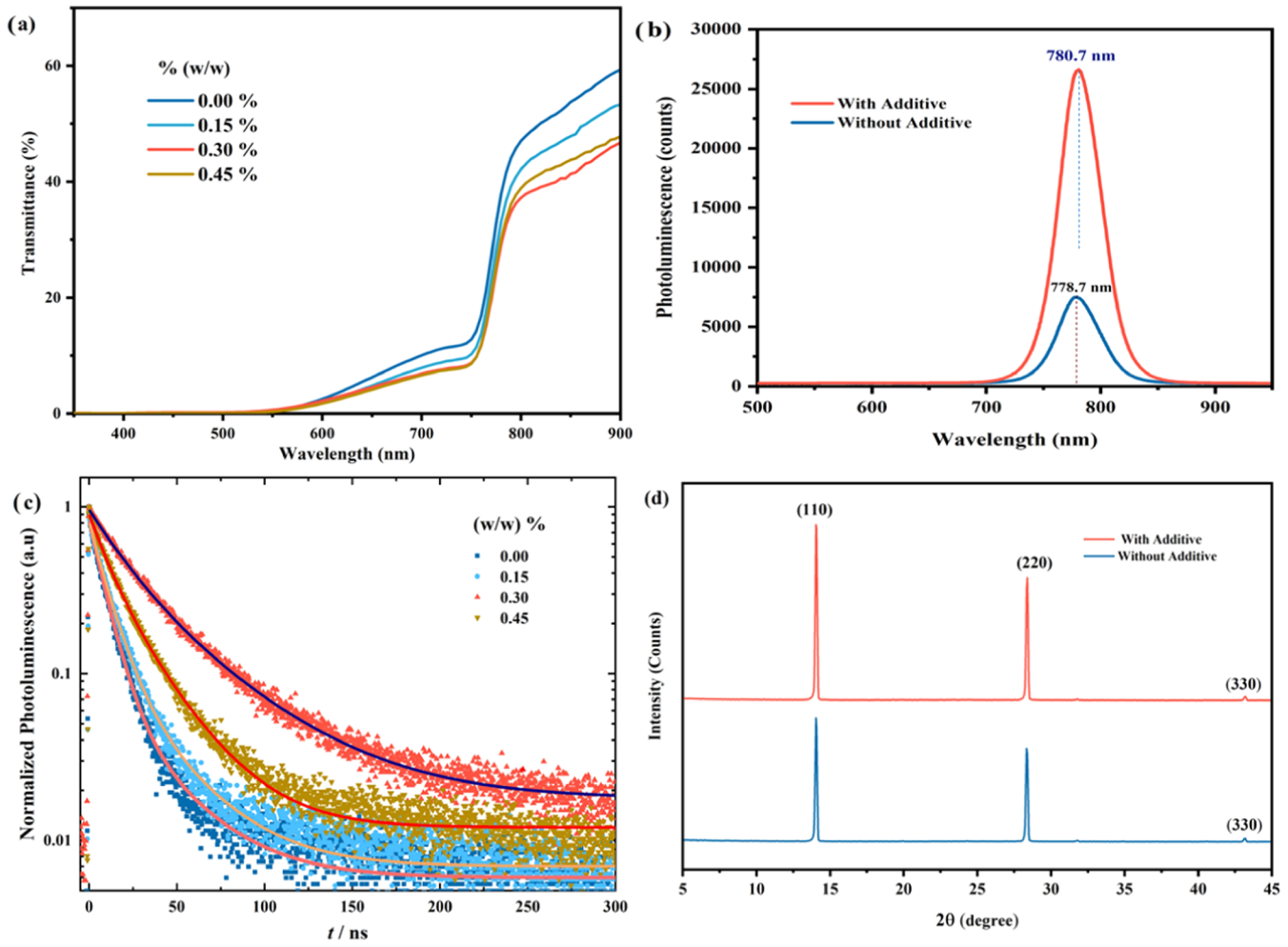

Figure 4. Optical properties of $MAPbI_3$ films with and without the 3-TMA additive. (a) UV−vis transmittance spectra, (b) time-resolved photoluminescence, (c) room-temperature photoluminescence, and (d) X-ray diffraction (XRD) of $MAPbI_3$ films with and without the 3-TMA additive.

strengths are dependent on the electron density and the bond length of the two nuclei between atoms.[53] In this regard, the corresponding bond lengths, which are calculated for non-covalent interactions, are larger than those of the covalent. This shows that the relative electron density that was calculated between atoms for NCI is smaller (Table S2). Consequently, theoretically extracted NCI between atoms of lead halides and 3-TMA is an important factor to regulate the crystallization kinetics of the OIHP thin films.[54]

3.1.2. Experimental Results. The ionic nature of OIHP thin films induces dissolution in moisturized environments even if a very small amount of water as a Lewis base is integrated into them.[55] To support such findings, the formation of hydrogen bonding with the organic or halides of OIHP thin films in the presence of water molecules, leading to chemical decomposition, was computationally studied.[56] One of the critical problems with OIHPSCs is their instability when exposed to moisture. To mitigate this kind of negative impact, improving the crystallinity of the photoactive layer or passivating surfaces or interfaces has been widely applied as a possible solution. In this work, water contact angle measurements were taken to examine the interaction of light-absorbing layers with water. The results in Figure 3a,b indicate that the hydrophobicity of the film with the additive is increased compared to that of the one without the additive, which attributes to the improved crystallinity and reduced trap-assisted recombination. Correspondingly, FTIR measurements were collected to investigate whether functional groups of 3-TMA interacted as a Lewis base with Pb^{2+}, which is a Lewis acid, to form a Lewis acid−base adduct or not. Figure 3c confirms that there is a shift to lower wavenumbers, which ascribes to the binding of two different C═O stretching vibrations from 1752 and 1680 to 1723 and 1638 cm^{-1} with PbI_2 to form a Lewis acid−base adduct. X-ray photoelectron spectroscopy (XPS) measurements were also conducted to further investigate the interaction of Pb^{2+} with the 3-TMA additive. In order to show the Pb 4f fitted peak spectra, the binding energy of Pb(0) is referenced (Figure S2a). Figure 3d shows the characteristic XPS spectra of fitted peaks of Pb 4f that shifts to a higher binding energy, which indicates the binding of uncoordinated Pb^{2+} with the carbonyl groups of the additive. In addition, the chemical shift of I 3d to a lower binding energy confirms hydrogen bonding interactions between the I^- and OH functional groups of additives (Figure 3e). This phenomenon is supported by the disappearance of the characteristic broad OH stretching peak of 3-TMA in the range of 3500−2500 cm^{-1} for the PbI_2 + 3-TMA sample (Figure S2). Moreover, C 1s also shows the change in the atomic mass percentage of carbon and the chemical shift in carboxyl groups with and without additives (Figure S2b,c). The chemical shift with a

https://doi.org/10.1021/acsomega.3c07592
ACS Omega 2024, 9, 2674−2686

lower binding energy in both cases is attributed to the increase in electron density and the decrease in electron affinity after more electrons are donated from carboxyl functional groups of the 3-TMA additive. In addition to this, the XPS results ensure that there is no leftover chlorine in the OIHP thin films.[57] Even though lone pair electrons on the sulfur atom have the possibility to bind with Pb^{2+}, the aromaticity of the thiophene could reduce the nucleophilicity of the sulfur atom. In addition, the seven-membered chelate ring, which is formed by Pb^{2+} and lone pair electrons of sulfur and oxygen, is less stable than the six-membered ring, which is formed by Pb^{2+} and lone pair electrons of oxygen in 3-TMA. Results obtained from the contact angle, FTIR, and XPS measurements confirm the existence of the interactions between Pb^{2+} and I^- with 3-TMA, which is consistent with the NCI findings from theoretical calculations. Therefore, the existing interactions are among the prominent elements that regulate the crystallization growth of OMHP thin films to improve the crystallinity and reduce SRH recombination.

3.2. Optical and Crystallographic Responses. The measured transmittance spectra (Figure 4a) of glass/ITO/PEDOT/OIHP films show that the transmittance of light is lowered for films with additives, which correlates to the formation of good crystals.[58] This, in turn, enhances the light-harvesting potential of the photoactive layer, which results in the generation of more charge carriers. Moreover, this phenomenon improves the charge collection efficiency of the OIHPSC.[59]

To study charge recombination dynamics, which strongly affect the whole performance of the solar cells as well as the quality of the light absorber layer, films with the glass/ITO/PEDOT:PSS/OIHP structure were prepared. The photoluminescence (PL) and time-resolved photoluminescence (TRPL) measurements were recorded in order to scrutinize the degree of defects in the absorber layer. It is well-known that the generation of electron−hole pairs by light absorption in solar cells is interconnected with the strong radiative recombination of the electron−hole pairs in a light-emitting diode.[60] As a result, the higher PL intensity (Figure 4b) after the addition of 3-TMA as the solid additive in the pristine OIHP solution proves that the trap-assisted nonradiative recombination is reduced due to the passivation of uncoordinated Pb^{2+} ions.[61] Similarly, TRPL spectroscopy measurements were collected to analyze the level of trap-assisted recombination. The TRPL curves are well fitted with a biexponential decay equation: $f(t) = A_1 \exp(-t/\tau_1) + A_2 \exp(-t/\tau_2) + B$, where τ_1 and τ_2 are the decay time constants of fast and slow processes, respectively, while A_1 and A_2 are corresponding to relative decay amplitudes of fast and slow processes, respectively, and B is the constant for the baseline offset.[62] The OIHP film without additives shows a distinctive biexponential fast TRPL decay process (τ_1), which indicates the presence of significant non-radiative recombination in the light absorber perovskite surface (Figure 4c and Table 1). On the other hand, the mentioned figure and table show that films with additives present longer lifetime decay than those without additives, which attributes to a lower density of the electron or hole-trapping centers. The extracted longer average decay time constant (τ_{avg}) also unveils that the reduced defect density in additive-treated OIHP films can be accounted for improved V_{oc} and FF.[63] In general, the longer radiative recombination (τ_2) pathways in the photoactive perovskite layer lead to an improvement of charge carrier injection, which contributes to enhancing photovoltaic characteristics like V_{oc}, J_{sc}, and FF of the OIHPSCs.

Table 1. Summary Decay of Relative Amplitudes, Time Constants, and Average Constant Time Extracted from Resolved Photoluminescence Spectra of Perovskite Films With and Without the 3-TMA Additive

w/w (%)	A_1	A_2	τ_1 (ns)	τ_2 (ns)	τ_{avg} (ns)
0.00	0.754	0.076	8.54	31.41	10.64
0.15	0.687	0.118	9.89	31.26	13.02
0.30	0.531	0.414	19.42	48.13	31.99
0.45	0.480	0.415	10.68	26.79	18.15

On the other hand, X-ray diffraction (XRD) measurements were carried out to analyze the effect of the 3-TMA additive on the crystal structure and phase of $MAPbI_3$. XRD spectra (Figure 4d) are presented for $MAPbI_3$ films with and without additives deposited on the glass substrate. The incorporation of additives did not change the tetragonal crystal phase of $MAPbI_3$ compared to the pristine film, which shows typical peaks at about 14.12, 28.43, and 43.23°, corresponding to the (110), (220), and (330) crystal planes, respectively.[64] But the equimolar excess CH_3NH_3I in both the precursor solution can remove residual PbI_2 from the surface of the photoactive perovskite layer;[65] therefore, the characteristic diffraction peak of residual PbI_2 at about 12.7° was not observed. Thus, the increased intensity of 3-TMA additive-treated $MAPbI_3$ films by ∼1.41 indicates that the crystal quality is improved, which is in good correlation with UV−vis−NIR, PL, and TRPL findings.

3.3. Topographic Profile. Atomic force microscopy (AFM) and scanning electron microscopy (SEM) imaging are employed to assess the morphology of $MAPbI_3$ films with and without 3-TMA. The sample films have a glass/ITO/PEDOT:PSS/OIHP configuration. Figure 5a,b indicates the AFM images of the films without and with additives, respectively. The OIHP films without and with additives have a root-mean-square roughness (R_q) of 36.2 and 23.3 nm, respectively. The lower R_q for the additive-incorporated film indicates that the additive improves the smoothness of the film, indicating reduced defect density on the surface of the film. The average grain sizes of films without and with additives are 1114 and 1355 nm, respectively (Figure S3a,b). The increment in average grain size due to the integration of additives in a precursor solution improves charge carrier transport with less non-radiative recombination across a surface.[66,67] Similarly, the SEM images in Figure 5c,d show the OIHP films without and with additives, respectively. In this work, additive-containing OIHP films show a notable rise in crystal grain size (Figure S3c,d). Thus, the degree of formation of small grains, which act as charge carrier trap centers, is reduced.[68]

3.4. Photovoltaic Characterization. In order to analyze the impact of 3-TMA on the mentioned photovoltaic parameters, current density−voltage (J−V) characteristics of perovskite solar cells having glass/ITO/PEDOT:PSS/OIHP/PCBM/TiOx/Al structures with a 0.15 cm^2 active cell area were measured under AM1.5 G (100 mW/cm^2) solar spectrum illumination. It is a well-known fact that charge carrier trapping centers or defects in OIHPSCs could be formed during film formation due to fast crystallization, which results in the formation of small grains.[69] Consequently, the performance of the solar device becomes poor owing to the reduced open-circuit voltage (V_{oc}), short-current density (J_{sc}), and fill factor (FF). That is why we used the additives to obtain optimal

https://doi.org/10.1021/acsomega.3c07592
ACS Omega 2024, 9, 2674−2686

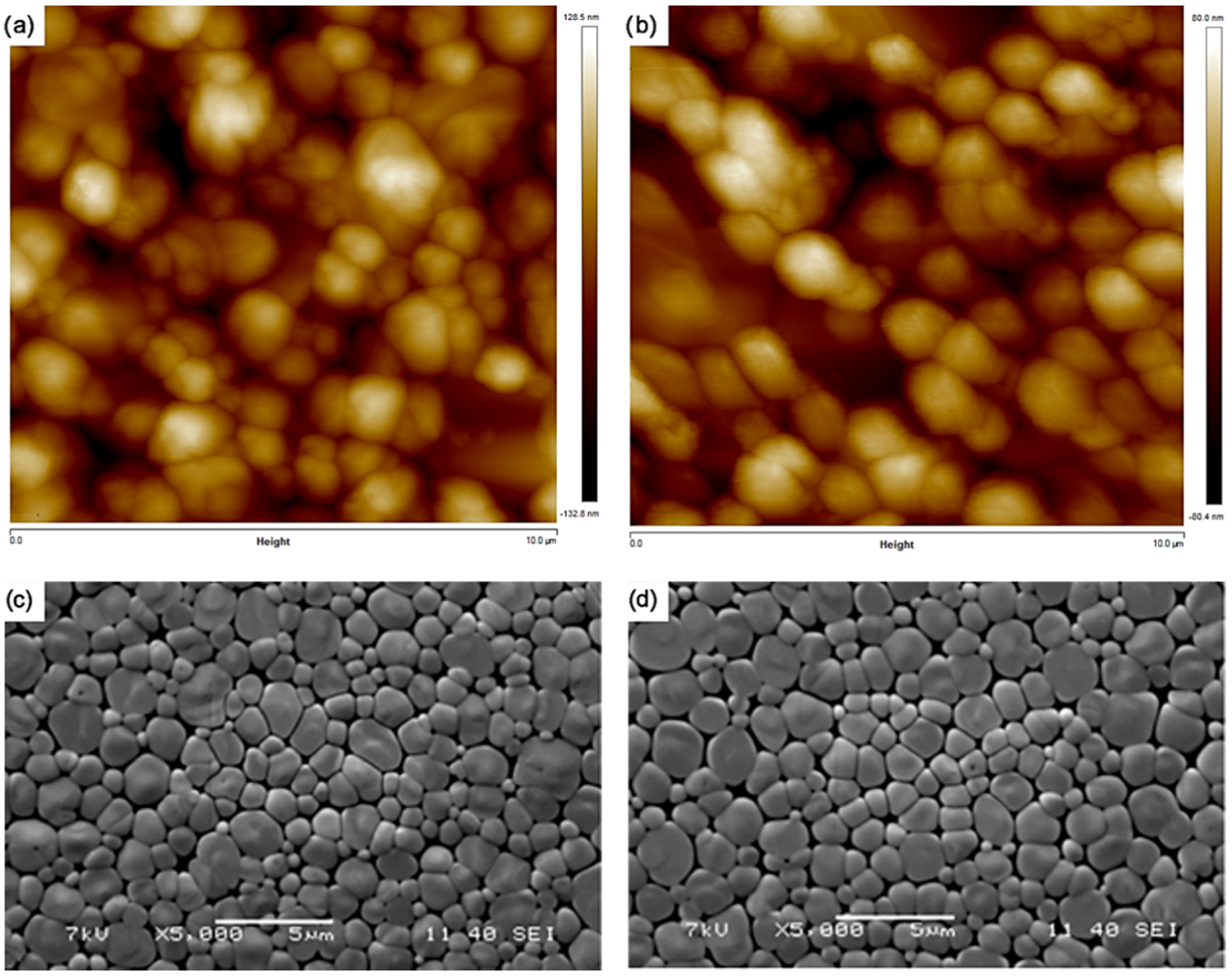

Figure 5. Topographic profile of $MAPbI_3$ films with and without 3-TMA. AFM images of $MAPbI_3$ films (a) without and (b) with additives. SEM images of films (c) without and (d) with additives.

morphology. To find the optimal concentration of the additive, the $J-V$ curves of about 30 $MAPbI_3$ devices with different percent concentrations (weight/weight), viz. 0.0, 0.15, 0.30, and 0.45 of 3-TMA, were compared. The characteristic $J-V$ curves in Figure 6a,b indicate that the additive with a 0.30% (w/w) concentration yields a maximum performance and less hysteresis. Statistical distribution of photovoltaic charteristics of the 61 additive-treated and 22 without additive devices is also plotted to compare the 3-TMA effect on the pristine solution (Figure S4(a–d)). Thus, when the additive was incorporated into the pristine solution, intriguing that improvements were observed in all $J-V$ characteristics, and also the optimum concentration of the additive shows small standard deviation for the cells. As mentioned in the discussion of optical and crystallographic responses and topographic profiles, the integration of additives enhanced the whole performance of a device either by regulating the kinetics of crystallization or weakening the surface defects in the material.[70] The plotted $J-V$ characteristics curves, the statistical distribution, and Table 2 indicate that V_{oc}, J_{sc}, and FF are improved when 0.30% (w/w) of the 3-TMA additive was added to the pristine, which attributes to the formation of a smooth surface and reduced nonradiative recombination.[42,71]

In addition, Figure 6c shows that the external quantum efficiency (EQE) and integrated J_{sc} are higher for the OIHPSCs containing 3-TMA. Additionally, the measured dark current–voltage response indicates that the leakage current is smaller for devices containing an additive, which could be attributed to the lowered trap-assisted Shockley–Read–Hall (SRH) recombination and high shunt resistance in the device (Figure 6d).[72,73] The results are consistent with $J-V$ curves (Figure 6a,b), attributing to the improved V_{oc}, J_{sc}, and FF of the additive-containing solar cells. Moreover, the continuous operational stability of encapsulated OIHPSCs was studied using the maximum power point tracking (MPPT) measurement under ambient conditions with a humidity of 40–50%. The PCE at MPPT (Figure 6e) indicates that the OIHPSC with 3-TMA shows improved stability compared to the control (devices without additives). The overall device characteristics indicate that the integration of additives during the solution preparation of the OIHPSCs improves the performance as well as stability of the device as a result of reduced SRH recombination.

To study the level of defect densities, space-charge-limited current (SCLC) measurements were used. The defect densities of the OIHPSCs with and without additives were explored by

https://doi.org/10.1021/acsomega.3c07592
ACS Omega 2024, 9, 2674–2686

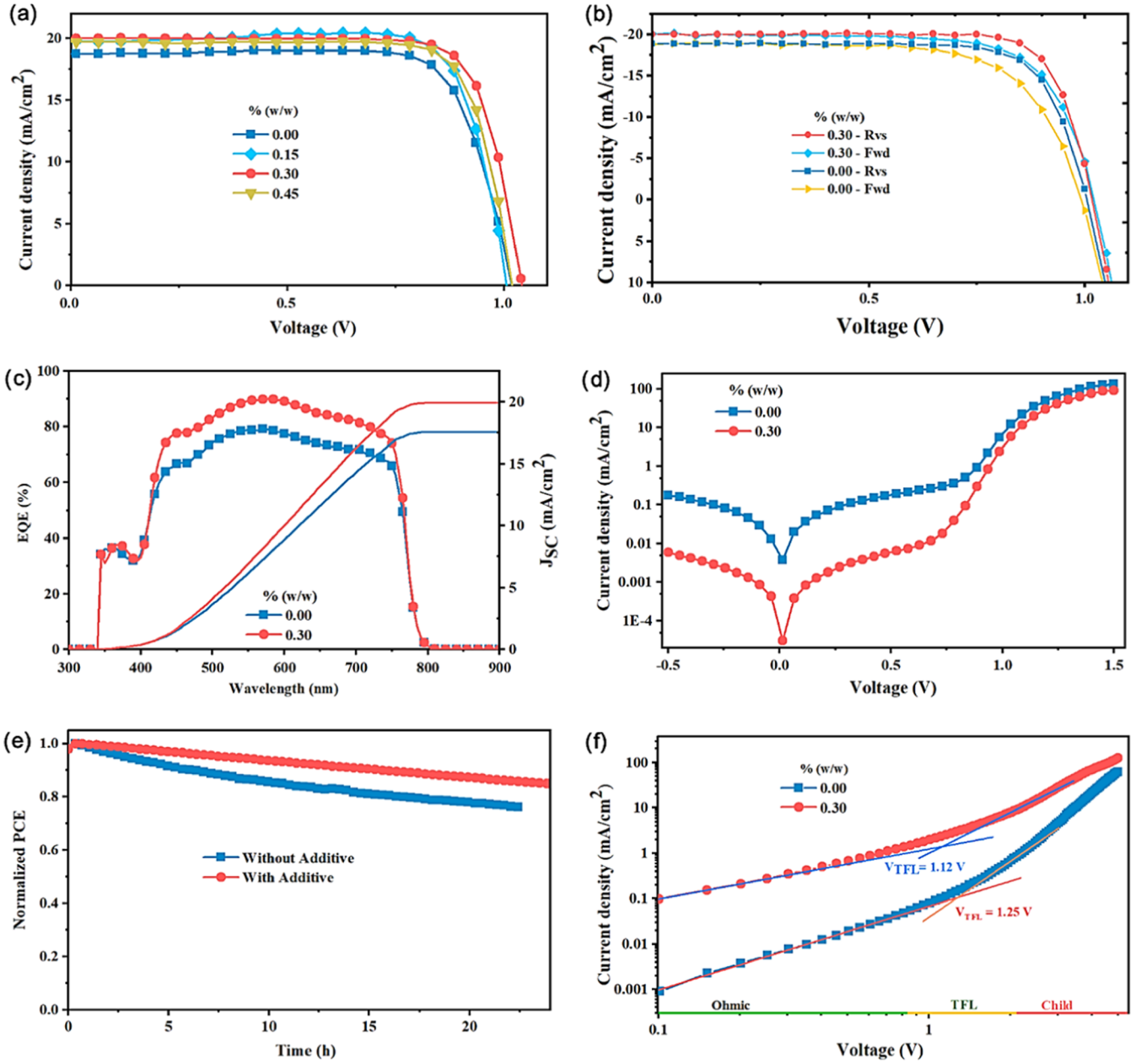

Figure 6. Photovoltaic properties of $MAPbI_3$ PSCs with and without additives. (a) Photocurrent density−voltage (J−V) characteristics of devices containing 0.00, 0.15, 0.30, and 0.45% (w/w) of 3-TMA. (b) J−V characteristics of reverse and forward scans of 0.00 and 0.30% (w/w), (c) external quantum efficiency (EQE) and integrated J_{sc}, and (d) semilog dark current−voltage curves of devices, incorporating 0.00 (control) and 0.30% (w/w) (optimized) of additives. (e) Normalized PCE obtained from maximum power point tracking (MPPT) measurements, and (f) dark J−V of hole-only devices incorporating 0.00 (control) and 0.30% (w/w) (optimized) of additives.

using the equation applied for trap-filled states.[74] Trap density (n_t) for hole-only devices having a glass/ITO/PEDOT:PSS/OIHP/PTAA/Al structure was calculated by using the $n_t = \frac{2V_{TFL}\varepsilon\varepsilon_0}{ed^2}$ equation, where V_{TFL} is the trap-filled limit voltage, ε is the relative dielectric constant of $CH_3NH_3PbI_3$ (ε = 32.2) of the perovskite, ε_0 is the vacuum permittivity constant, e is an elementary charge, and d is the thickness of the OIHP film. V_{TFL} is 1.25 and 1.12 V for the device without and with additives, respectively (Figure 6f). The calculated n_t for the device without additives (1.78×10^{16} cm^{-3}) is larger than the device with additives (1.60×10^{16} cm^{-3}), proving that the density of trapping densities in the film is reduced due to the incorporation of 3-TMA as the additive.

3.5. Charge Carrier Recombination Dynamics. To study the charge carrier recombination dynamics in the device, intensity-modulated photovoltaic spectroscopy (IMVS) was employed. The measurement was made in the absence of charge extraction in order to find the decay of charge carriers as a result of defects in OIHPSCs. In IMVS response, the dominant SRH recombination (recombination resistance) phenomena are mainly observed in the lower transfer function semicircle region of the Nyquist plot (Figure 7a), which is analogous to a lower frequency semicircle region in electrochemical impedance spectroscopy (EIS).[75] The finding shows that devices with additives exhibit enhanced recombination resistance compared with devices without additives.

https://doi.org/10.1021/acsomega.3c07592
ACS Omega 2024, 9, 2674−2686

Table 2. Summarized Photovoltaic Parameters (i.e., V_{oc}, J_{sc}, FF, and PCE) of $MAPbI_3$ PSCs With and Without Additives under 100 mW/cm^2 Light Intensity Illumination

% (w/w)		V_{oc} (V)	J_{sc} (mA/cm^2)	FF (%)	PCE (%)
0.00	av.	1.00 ± 0.03	18.7 ± 0.5	75.4 ± 2.8	14.0 ± 0.8
	best	1.02	18.7	77.7	14.9
0.15	av.	1.00 ± 0.01	19.5 ± 0.4	77.9 ± 1.9	15.3 ± 0.5
	best	1.01	19.8	80.9	16.1
0.30	av.	1.01 ± 0.02	19.7 ± 0.4	79.4 ± 1.3	15.8 ± 0.4
	best	1.04	20.0	79.2	16.5
0.45	av.	1.00 ± 0.01	19.0 ± 0.8	78.8 ± 1.4	15.0 ± 0.6
	best	1.02	19.7	79.1	15.9

Figure 7b represents the imaginary transfer function (H'') vs frequency, which was scanned in the range of 1 MHz to 50 mHz with 10% light intensity modulation amplitude under 8 mW/cm^2 LED light intensity. The critical frequency (f_c) $\left(f_c = \frac{1}{2\pi\tau_c}\right)$ is directly related to the maximum of H'' at a high frequency and inversely proportional to the time constant (τ_c). The time constants for devices with additives are longer than those without additives, which suggests a lower charge recombination rate in additive-incorporated devices.[76,77] Moreover, the ideality factor (n_{id}), which is calculated from the slope of the graph of V_{oc} as a function of light illumination intensity (Figure 7c), suggests the presence of trap-assisted recombination in the devices.[78,79] The extracted n_{id} values for the OIHPSCs with 0.30% (w/w) and without additives are ∼1.34 and ∼1.39, respectively. The results infer that the improved V_{oc} of additives containing OIHPSCs is attributed to the reduced trap-assisted recombination and high shunt resistance of devices.[77,80]

The recombination time constant versus light illumination intensity graph (Figure 7d) was plotted to compare the recombination time constant of the OIHPSCs with and without additives. Devices with additives show a longer recombination lifetime compared to devices without additives, which attributes to suppressed trap-assisted recombination and improved charge extraction processes across device interfaces.

4. CONCLUSIONS

The findings in this work show that the integration of 3-TMA as a solid additive to the precursor perovskite solution has the potential to bind its carbonyl groups (Lewis base) to Pb^{2+} (Lewis acid). Its binding potential simplifies the free charge carrier mobility and extraction across the bulk and interface of the OIHP layer.[5,81,82] Consequently, the additive-incorporated p-i-n OIHPSC, which was processed in an ambient environment except for top contact, showed significant improvements in V_{oc}, J_{sc}, FF, and stability of the device. The results confirm that the incorporation of this additive is a viable strategy to reduce trap-assisted recombination and improve the overall performance of $MAPbI_3$-based perovskite solar cells.

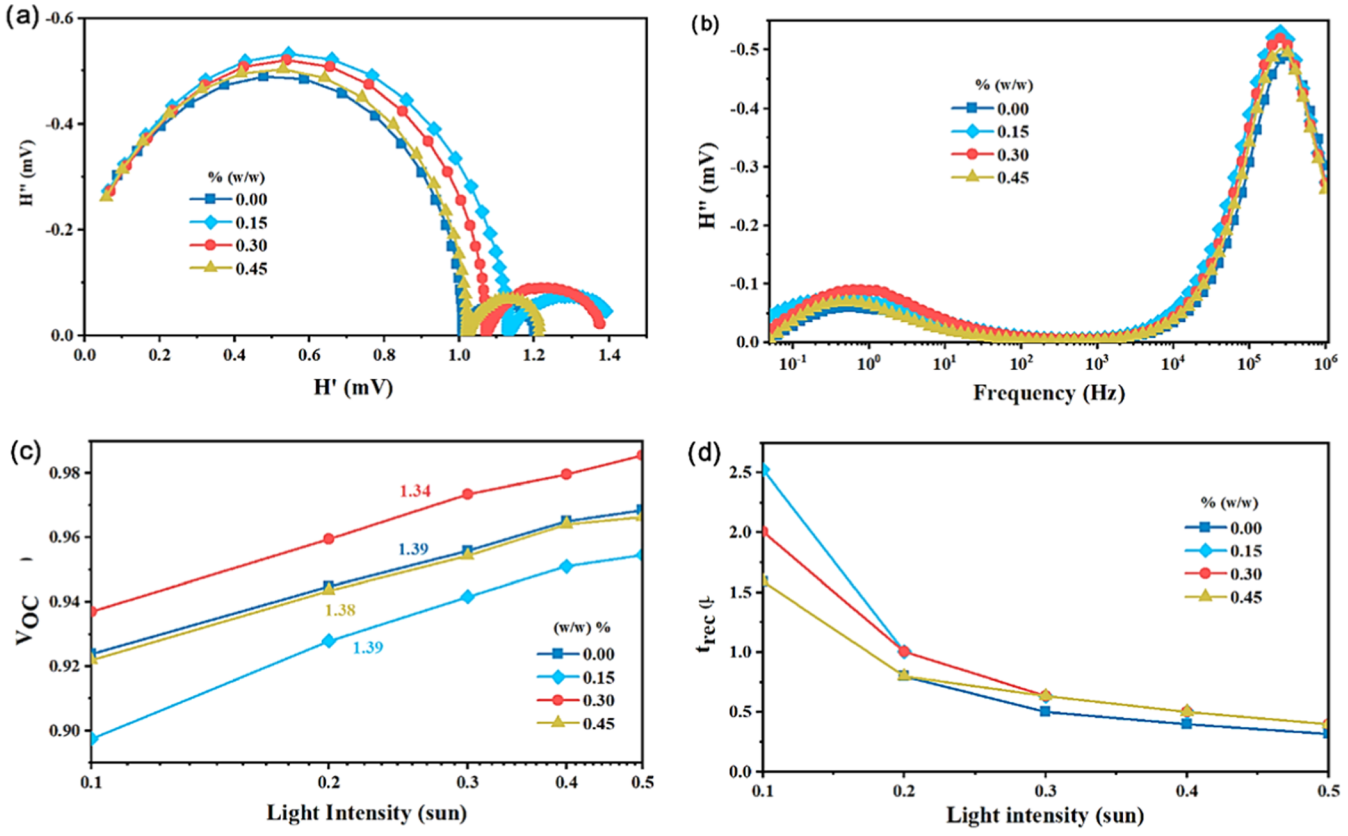

Figure 7. Intensity-modulated photovoltage characteristics of $MAPbI_3$ PSCs containing 0, 0.15, 0.3, and 0.45% (w/w) of the 3-TMA additive. (a) Nyquist plots, (b) imaginary transfer function (H'') vs frequency plots, (c) open-circuit voltage (V_{oc}) as a function of photon flux (cm^{-2} s^{-1}) intensity, and (d) charge carrier recombination time constant (τ_{IMVS}) as a function of V_{oc} of OIHPSCs.

https://doi.org/10.1021/acsomega.3c07592
ACS Omega 2024, 9, 2674−2686

■ ASSOCIATED CONTENT

Data Availability Statement

The data that support the plots within this paper and other findings of this study are available from the corresponding author upon request.

Supporting Information

The Supporting Information is available free of charge at https://pubs.acs.org/doi/10.1021/acsomega.3c07592.

Relative energies of the configurations calculated using M06-2X/6-31+G(d,p) and LANI2DZ (Table S1); electron density parameters at bond critical points (BCPs) (Table S2); HOMO of 3-thiophenemalenoic acid (Figure S1); FTIR spectra of 3-TMA and $MAPbI_3$ with 3-TMA (Figure S2); XPS spectra of C 1s (Figure S3); grain size distribution of $MAPbI_3$ and $MAPbI_3$ with 3-TMA (Figure S4); statistical distribution of $J-V$ characteristics (Figure S5); maximum power point tracking (MPPT) under continuous operation (Figure S2); and source data (PDF)

■ AUTHOR INFORMATION

Corresponding Author

Getachew Adam Workneh − *Department of Industrial Chemistry, Addis Ababa Science and Technology University, 16417 Addis Ababa, Ethiopia; Sustainable Energy Center of Excellence, Addis Ababa Science and Technology University, 16417 Addis Ababa, Ethiopia;* orcid.org/0000-0002-2863-1379; Email: getachew.adam@aastu.edu.et

Authors

Samuel Abicho − *Department of Industrial Chemistry, Addis Ababa Science and Technology University, 16417 Addis Ababa, Ethiopia; Sustainable Energy Center of Excellence, Addis Ababa Science and Technology University, 16417 Addis Ababa, Ethiopia; Linz Institute for Organic Solar Cells (LIOS)/Institute of Physical Chemistry, Johannes Kepler University, Linz, 4040 Linz, Austria; Department of Chemistry, Hawassa University, 05 Hawassa, Ethiopia*

Bekele Hailegnaw − *Division of Soft Matter Physics and LIT Soft Materials Lab, Johannes Kepler University, Linz, 4040 Linz, Austria;* orcid.org/0000-0003-4427-2772

Felix Mayr − *Linz Institute for Organic Solar Cells (LIOS)/Institute of Physical Chemistry, Johannes Kepler University, Linz, 4040 Linz, Austria*

Munise Cobet − *Linz Institute for Organic Solar Cells (LIOS)/Institute of Physical Chemistry, Johannes Kepler University, Linz, 4040 Linz, Austria*

Cigdem Yumusak − *Linz Institute for Organic Solar Cells (LIOS)/Institute of Physical Chemistry, Johannes Kepler University, Linz, 4040 Linz, Austria*

Teshome Abute Lelisho − *Department of Chemistry, Hawassa University, 05 Hawassa, Ethiopia*

Teketel Yohannes − *Department of Chemistry, Addis Ababa University, 1176 Addis Ababa, Ethiopia*

Martin Kaltenbrunner − *Division of Soft Matter Physics and LIT Soft Materials Lab, Johannes Kepler University, Linz, 4040 Linz, Austria*

Niyazi Serdar Sariciftci − *Linz Institute for Organic Solar Cells (LIOS)/Institute of Physical Chemistry, Johannes Kepler University, Linz, 4040 Linz, Austria;* orcid.org/0000-0003-4727-1193

Markus Clark Scharber − *Linz Institute for Organic Solar Cells (LIOS)/Institute of Physical Chemistry, Johannes Kepler University, Linz, 4040 Linz, Austria;* orcid.org/0000-0002-4918-4803

Complete contact information is available at: https://pubs.acs.org/10.1021/acsomega.3c07592

Notes

The authors declare no competing financial interest.

■ ACKNOWLEDGMENTS

The authors would like to acknowledge Erasmus+ KA107 (project number 2020-1-AT01-KA107-077800), Linz Institute for Organic Solar cells (LIOS), Johannes Kepeler University, Linz, Austria, Africa Uninet and OeAD-GmbH−Austria's Agency for Education and Internationalization, Austria Addis Ababa Science and Technology University, Addis Ababa, Ethiopia, and Hawassa University, Hawassa, Ethiopia, for their financial, material, and laboratory support.

■ REFERENCES

(1) Kojima, A.; Teshima, K.; Shirai, Y.; Miyasaka, T. Organometal Halide Perovskites as Visible-Light Sensitizers for Photovoltaic Cells. *J. Am. Chem. Soc.* **2009**, *131* (17), 6050−6051.

(2) National renewable Energy Laboratory (NREL) Best Research-Cell Efficiencies, 2023 http://www.nrel.gov/ncpv/images/efficiency_chart.jpg.

(3) Liang, Z.; Bi, Z.; Gao, K.; Fu, Y.; Guan, P.; Feng, X.; Chai, Z.; Xu, G.; Xu, X. Interface Modification via Al_2O_3 with Retarded Charge Recombinations for Mesoscopic Perovskite Solar Cells Fabricated with Spray Deposition Process in the Air. *Appl. Surf. Sci.* **2019**, *463*, 939−946.

(4) Baranowski, M.; Plochocka, P. Excitons in Metal-Halide Perovskites. *Adv. Energy Mater.* **2020**, *10* (26), No. 1903659.

(5) Abicho, S.; Hailegnaw, B.; Workneh, G. A.; Yohannes, T. Role of Additives and Surface Passivation on the Performance of Perovskite Solar Cells. *Mater. Renewable Sustainable Energy* **2022**, *11*, 47−70, DOI: 10.1007/s40243-021-00206-9.

(6) Baumann, A.; Väth, S.; Rieder, P.; Heiber, M. C.; Tvingstedt, K.; Dyakonov, V. Identification of Trap States in Perovskite Solar Cells. *J. Phys. Chem. Lett.* **2015**, *6* (12), 2350−2354.

(7) Wu, X.; Trinh, M. T.; Niesner, D.; Zhu, H.; Norman, Z.; Owen, J. S.; Yaffe, O.; Kudisch, B. J.; Zhu, X. Y. Trap States in Lead Iodide Perovskites. *J. Am. Chem. Soc.* **2015**, *137* (5), 2089−2096.

(8) Berdiyorov, G. R.; Madjet, M. E.; El-Mellouhi, F.; Peeters, F. M. Effect of Crystal Structure on the Electronic Transport Properties of the Organometallic Perovskite $CH_3NH_3PbI_3$. *Sol. Energy Mater. Sol. Cells* **2016**, *148*, 60−66.

(9) Varadwaj, P. R.; Varadwaj, A.; Marques, H. M.; Yamashita, K. Significance of Hydrogen Bonding and Other Noncovalent Interactions in Determining Octahedral Tilting in the $CH_3NH_3PbI_3$ Hybrid Organic-Inorganic Halide Perovskite Solar Cell Semiconductor. **2019**, *9*.

(10) Brivio, F.; Frost, J. M.; Skelton, J. M.; Jackson, A. J.; Weber, O. J.; Weller, M. T.; Goñi, A. R.; Leguy, A. M. A.; Barnes, P. R. F.; Walsh, A. Lattice Dynamics and Vibrational Spectra of the Orthorhombic, Tetragonal, and Cubic Phases of Methylammonium Lead Iodide. *Phys. Rev. B* **2015**, *92* (14), No. 144308.

(11) Wang, S.; Sina, M.; Parikh, P.; Uekert, T.; Shahbazian, B.; Devaraj, A.; Meng, Y. S. Role of 4-Tert-Butylpyridine as a Hole Transport Layer Morphological Controller in Perovskite Solar Cells. *Nano Lett.* **2016**, *16* (9), 5594−5600.

(12) Jeon, N. J.; Noh, J. H.; Yang, W. S.; Kim, Y. C.; Ryu, S.; Seo, J.; Seok, S. Il. Compositional Engineering of Perovskite Materials for High-Performance Solar Cells. *Nature* **2015**, *517* (7535), 476−480.

(13) Jung, K.; Chae, W.; Choi, J. W.; Kim, K. C.; Lee, M. Synergistic Passivation of $MAPbI_3$ Perovskite Solar Cells by Compositional Engineering Using Acetamidinium Bromide Additives. *J. Energy Chem.* **2021**, *59*, 755−762.
(14) Pereyra, C.; Xie, H.; Lira-Cantu, M. Additive Engineering for Stable Halide Perovskite Solar Cells. *J. Energy Chem.* **2021**, *60*, 599−634.
(15) Elsenety, M. M.; Christopoulos, E.; Falaras, P. Passivation Engineering Using Ultrahydrophobic Donor−π−Acceptor Organic Dye with Machine Learning Insights for Efficient and Stable Perovskite Solar Cells. *Sol. RRL* **2023**, *7* (10), No. 2201016.
(16) Hailegnaw, B.; Adam, G.; Wielend, D.; Pedarnig, J. D.; Sariciftci, N. S.; Scharber, M. C. Acetylacetone Improves the Performance of Mixed Halide Perovskite Solar Cells. *J. Phys. Chem. C* **2019**, *123* (39), 23807−23816.
(17) Xia, J.; Liang, C.; Gu, H.; Mei, S.; Li, S.; Zhang, N.; Chen, S.; Cai, Y.; Xing, G. Surface Passivation Toward Efficient and Stable Perovskite Solar Cells. *Energy Environ. Mater.* **2023**, *6* (1), No. e12296.
(18) Lee, S. J.; Cheng, H. C.; Wang, Y.; Zhou, B.; Li, D.; Wang, G.; Liu, Y.; Guo, J.; Wu, H.; Kang, D. J.; Huang, Y.; Duan, X. Lead Halide Perovskite Sensitized WSe_2 Photodiodes with Ultrahigh Open Circuit Voltages. *eLight* **2023**, *3*, No. 8.
(19) Li, H.; Wang, Y.; Gao, H.; Zhang, M.; Lin, R.; Wu, P.; Xiao, K.; Tan, H. Revealing the Output Power Potential of Bifacial Monolithic All-Perovskite Tandem Solar Cells. *eLight* **2022**, *2* (1), No. 21.
(20) Hartono, N. T. P.; Sun, S.; Gélvez-Rueda, M. C.; Pierone, P. J.; Erodici, M. P.; Yoo, J.; Wei, F.; Bawendi, M.; Grozema, F. C.; Sher, M. J.; Buonassisi, T.; Correa-Baena, J. P. The Effect of Structural Dimensionality on Carrier Mobility in Lead-Halide Perovskites. *J. Mater. Chem. A* **2019**, *7* (41), 23949−23957.
(21) Liang, C.; Gu, H.; Xia, Y.; Wang, Z.; Liu, X.; Xia, J.; Zuo, S.; Hu, Y.; Gao, X.; Hui, W.; Chao, L.; Niu, T.; Fang, M.; Lu, H.; Dong, H.; Yu, H.; Chen, S.; Ran, X.; Song, L.; Li, B.; Zhang, J.; Peng, Y.; Shao, G.; Wang, J.; Chen, Y.; Xing, G.; Huang, W. Two-Dimensional Ruddlesden−Popper Layered Perovskite Solar Cells Based on Phase-Pure Thin Films. *Nat. Energy* **2021**, *6*, 38−45.
(22) Lewis, D. J. Deposition Techniques for Perovskite Solar Cells. In *Nanostructured Materials for Type III Photovoltaics*; The Royal Society of Chemistry: U.K., 2018; pp 341−366.
(23) Wang, F.; Ge, C.; Zhou, X.; Liang, X.; Duan, D.; Lin, H.; Zhu, Q.; Hu, H. Manipulation of Crystallization Kinetics for Perovskite Photovoltaics Prepared Using Two-Step Method. *Crystals* **2022**, *12*, No. 815.
(24) Wang, S.; Wang, A.; Deng, X.; Xie, L.; Xiao, A.; Li, C.; Xiang, Y.; Li, T.; Ding, L.; Hao, F. Lewis Acid/Base Approach for Efficacious Defect Passivation in Perovskite Solar Cells. *J. Mater. Chem. A* **2020**, *8* (25), 12201−12225.
(25) Amrollahi, H.; Moshaii, A.; Borhani, M.; Xu, X.; Chueh, C.; Yang, Z.; Rajagopal, A.; Xu, J.; Byeok, S.; Jen, A. K.; Santhosh, N.; Daniel, R. I.; Acchutharaman, K. R.; Pandian, M. S.; Ramasamy, P.; Patil, J. V.; Park, D. W.; Hee, Y.; Wu, W.; Yang, Z.; Rudd, P. N.; Shao, Y.; Dai, X.; Wei, H.; Almora, O.; Baran, D.; Bazan, G. C.; Berger, C.; Cabrera, C. I.; Catchpole, K. R.; Erten-ela, S.; Guo, F.; Hauch, J.; Ho-baillie, A. W. Y.; Jacobsson, T. J.; Janssen, R. A. J.; Kirchartz, T.; Kopidakis, N.; Li, Y.; Loi, M. A.; Lunt, R. R.; Mathew, X.; Mcgehee, M. D.; Min, J.; Mitzi, D. B.; Nazeeruddin, M. K.; Nelson, J.; Nogueira, A. F.; Paetzold, U. W.; Park, N.; Rand, B. P.; Rau, U.; Snaith, H. J.; Unger, E.; Vaillant-roca, L.; Yip, H.; Brabec, C. J.; Zhang, Z. L.; Men, B. Q.; Liu, Y. F.; Gao, H. P.; Mao, Y. L.; Chen, B.; Rudd, P. N.; Yang, S.; Huang, J.; Rudd, P. N.; Afroz, M. A.; Garai, R.; Gupta, R. K.; Iyer, P. K.; Nh, C. H.; Cl, P.; Wang, W.; Zhang, Z. L.; Cai, Y.; Chen, J.; Wang, J.; Huang, R.; Lu, X.; Phys, A.; Ananda, W.; Chen, B.; Rudd, P. N.; Yang, S.; Huang, J.; Rudd, P. N. Chem Soc Rev Imperfections and Their Passivation in Halide Perovskite Solar Cells. *Synth. Met.* **2019**, *283*, No. 116965.
(26) Zhu, X.; Lin, R.; Gu, H.; Hu, H. C.; Liu, Z.; Xing, G.; Wu, Y.; Ouyang, X. Ecofriendly Hydroxyalkyl Cellulose Additives for Efficient and Stable $MAPbI_3$-Based Inverted Perovskite Solar Cells. *Energy Environ. Mater.* **2023**, *6*, No. e12426.
(27) He, Z.; Hu, Y.; Yu, Z.; Jia, X.; Zhang, S.; Tao, Q.; Zhao, W.; Wu, Y.; Xu, Q.; Jiao, M.; Wang, D.; Yang, C. A Multifunctional Flame Retardant Enabling Efficient and Stable Formamidine-Cesium Perovskite Solar Cells. *Sol. Energy Mater. Sol. Cells* **2022**, *238*, No. 111641.
(28) Ma, H.; Zhang, H.; Wang, L.; Song, M. Application of Ethyl Acetoacetate Bifocal Additive for Achieving High-Performance Perovskite Solar Cells. *Mater. Sci. Semicond. Process.* **2023**, *153*, No. 107130.
(29) Gupta, R. K.; Garai, R.; Iyer, P. K. Ambient Stable Perovskite Solar Cells through Trifluoro Acetic Acid-Mediated Multifunctional Anchoring. *ACS Appl. Energy Mater.* **2022**, *5* (2), 1571−1579.
(30) Baranwal, A. K.; Nishimura, K.; Liu, D.; Kamarudin, M. A.; Kapil, G.; Saini, S.; Yabuki, T.; Iikubo, S.; Minemoto, T.; Yoshino, K.; Miyazaki, K.; Shen, Q.; Hayase, S. Relationship between Carrier Density and Precursor Solution Stirring for Lead-Free Tin Halide Perovskite Solar Cells Performance. *ACS Appl. Energy Mater.* **2022**, *5* (4), 4002−4007.
(31) Yukta; Chavan, R. D.; Prochowicz, D.; Yadav, P.; Tavakoli, M. M.; Satapathi, S. Thiocyanate-Passivated Diaminonaphthalene-Incorporated Dion-Jacobson Perovskite for Highly Efficient and Stable Solar Cells. *ACS Appl. Mater. Interfaces* **2022**, *14* (1), 850−860.
(32) Burschka, J.; Pellet, N.; Moon, S. J.; Humphry-Baker, R.; Gao, P.; Nazeeruddin, M. K.; Grätzel, M. Sequential Deposition as a Route to High-Performance Perovskite-Sensitized Solar Cells. *Nature* **2013**, *499* (7458), 316−319.
(33) Park, S. H.; Roy, A.; Beaupré, S.; Cho, S.; Coates, N.; Moon, J. S.; Moses, D.; Leclerc, M.; Lee, K.; Heeger, A. J. Bulk Heterojunction Solar Cells with Internal Quantum Efficiency Approaching 100%. *Nat. Photonics* **2009**, *3*, 297−303.
(34) Adam, G.; Kaltenbrunner, M.; Głowacki, E. D.; Apaydin, D. H.; White, M. S.; Heilbrunner, H.; Tombe, S.; Stadler, P.; Ernecker, B.; Klampfl, C. W.; Sariciftci, N. S.; Scharber, M. C. Solution Processed Perovskite Solar Cells Using Highly Conductive PEDOT:PSS Interfacial Layer. *Sol. Energy Mater. Sol. Cells* **2016**, *157*, 318−325.
(35) Ouyang, J.; Xu, Q.; Chu, C. W.; Yang, Y.; Li, G.; Shinar, J. On the Mechanism of Conductivity Enhancement in Poly(3,4-Ethylenedioxythiophene):Poly(Styrene Sulfonate) Film through Solvent Treatment. *Polymer* **2004**, *45* (25), 8443−8450.
(36) McGettrick, J. D.; Hooper, K.; Pockett, A.; Baker, J.; Troughton, J.; Carnie, M.; Watson, T. Sources of Pb(0) Artefacts during XPS Analysis of Lead Halide Perovskites. *Mater. Lett.* **2019**, *251* (0), 98−101.
(37) Zhao, Y.; Truhlar, D. G. The M06 Suite of Density Functionals for Main Group Thermochemistry, Thermochemical Kinetics, Noncovalent Interactions, Excited States, and Transition Elements: Two New Functionals and Systematic Testing of Four M06-Class Functionals and 12 Other Function. *Theor. Chem. Acc.* **2008**, *120* (1−3), 215−241.
(38) Frisch, M. J.; Trucks, G. W.; Schlegel, H. B.; Scuseria, G. E.; Robb, M. A.; Cheeseman, J. R.; Scalmani, G.; Barone, V.; Mennucci, B.; Petersson, G. A.; Nakatsuji, H.; Caricato, M.; Li, X.; Hratchian, H. P.; Izmaylov, A. F.; Bloino, J.; Zheng, G.; Sonnenberg, J. L.; Hada, M.; Ehara, M.; Toyota, K.; Fukuda, R.; Hasegawa, J.; Ishida, M.; Nakajima, T.; Honda, Y.; Kitao, O.; Nakai, H.; Vreven, T.; Montgomery, J. A.; Peralta, J. E.; Ogliaro, F.; Bearpark, M.; Heyd, J. J.; Brothers, E.; Kudin, K. N.; Staroverov, V. N.; Kobayashi, R.; Normand, J.; Raghavachari, K.; Rendell, A.; Burant, J. C.; Iyengar, S. S.; Tomasi, J.; Cossi, M.; Rega, N.; Millam, J. M.; Klene, M.; Knox, J. E.; Cross, J. B.; Bakken, V.; Adamo, C.; Jaramillo, J.; Gomperts, R.; Stratmann, R. E.; Yazyev, O.; Austin, A. J.; Cammi, R.; Pomelli, C.; Ochterski, J. W.; Martin, R. L.; Morokuma, K.; Zakrzewski, V. G.; Voth, G. A.; Salvador, P.; Dannenberg, J. J.; Dapprich, S.; Daniels, A. D.; Farkas; Foresman, J. B.; Ortiz, J. V.; Cioslowski, J.; Fox, D. J. *Gaussian 09*. Revision B.01; Gaussian, Inc.: Wallingford CT, 2009.

https://doi.org/10.1021/acsomega.3c07592
ACS Omega 2024, 9, 2674−2686

(39) Hay, P. J.; Wadt, W. R. Ab Initio Effective Core Potentials for Molecular Calculations. Potentials for K to Au Including the Outermost Core Orbitale. *J. Chem. Phys.* **1985**, *82* (1), 299−310.
(40) Lu, T.; Chen, F. Multiwfn: A Multifunctional Wavefunction Analyzer. *J. Comput. Chem.* **2012**, *33* (5), 580−592.
(41) Humphrey, W.; Dalke, A.; Schulten, K. VMD: Visual Molecular Dynamics. *J. Mol. Graphics* **1996**, *14*, 33−38.
(42) Afroz, M. A.; Garai, R.; Gupta, R. K.; Iyer, P. K. Additive-Assisted Defect Passivation for Minimization of Open-Circuit Voltage Loss and Improved Perovskite Solar Cell Performance. *ACS Appl. Energy Mater.* **2021**, *4* (10), 10468−10476.
(43) Pearson, R. G. Recent Advances in the Concept of Hard and Soft Acids and Bases. *J. Chem. Educ.* **1987**, *64*, 561−567.
(44) Liu, X.; Cheng, Y.; Liu, C.; Zhang, T.; Zhang, N.; Zhang, S.; Chen, J.; Xu, Q.; Ouyang, J.; Gong, H. 20.7% Highly Reproducible Inverted Planar Perovskite Solar Cells with Enhanced Fill Factor and Eliminated Hysteresis. *Energy Environ. Sci.* **2019**, *12* (5), 1622−1633.
(45) Deng, X.; Cao, Z.; Yuan, Y.; Oliver Lam Chee, M.; Xie, L.; Wang, A.; Xiang, Y.; Li, T.; Dong, P.; Ding, L.; Hao, F. Coordination Modulated Crystallization and Defect Passivation in High Quality Perovskite Film for Efficient Solar Cells. *Coord. Chem. Rev.* **2020**, *420*, No. 213408.
(46) Jacobsson, T. J.; Hultqvist, A.; García-Fernández, A.; Anand, A.; Al-Ashouri, A.; Hagfeldt, A.; Crovetto, A.; Abate, A.; Ricciardulli, A. G.; Vijayan, A.; Kulkarni, A.; Anderson, A. Y.; Darwich, B. P.; Yang, B.; Coles, B. L.; Perini, C. A. R.; Rehermann, C.; Ramirez, D.; Fairen-Jimenez, D.; Di Girolamo, D.; Jia, D.; Avila, E.; Juarez-Perez, E. J.; Baumann, F.; Mathies, F.; González, G. S. A.; Boschloo, G.; Nasti, G.; Paramasivam, G.; Martínez-Denegri, G.; Näsström, H.; Michaels, H.; Köbler, H.; Wu, H.; Benesperi, I.; Dar, M. I.; Bayrak Pehlivan, I.; Gould, I. E.; Vagott, J. N.; Dagar, J.; Kettle, J.; Yang, J.; Li, J.; Smith, J. A.; Pascual, J.; Jerónimo-Rendón, J. J.; Montoya, J. F.; Correa-Baena, J. P.; Qiu, J.; Wang, J.; Sveinbjörnsson, K.; Hirselandt, K.; Dey, K.; Frohna, K.; Mathies, L.; Castriotta, L. A.; Aldamasy, M. H.; Vasquez-Montoya, M.; Ruiz-Preciado, M. A.; Flatken, M. A.; Khenkin, M. V.; Grischek, M.; Kedia, M.; Saliba, M.; Anaya, M.; Veldhoen, M.; Arora, N.; Shargaieva, O.; Maus, O.; Game, O. S.; Yudilevich, O.; Fassl, P.; Zhou, Q.; Betancur, R.; Munir, R.; Patidar, R.; Stranks, S. D.; Alam, S.; Kar, S.; Unold, T.; Abzieher, T.; Edvinsson, T.; David, T. W.; Paetzold, U. W.; Zia, W.; Fu, W.; Zuo, W.; Schröder, V. R. F.; Tress, W.; Zhang, X.; Chiang, Y. H.; Iqbal, Z.; Xie, Z.; Unger, E. An Open-Access Database and Analysis Tool for Perovskite Solar Cells Based on the FAIR Data Principles. *Nat. Energy* **2022**, *7* (1), 107−115.
(47) Wang, Z.; You, S.; Zheng, G.; Tang, Z.; Zhang, L.; Zhang, J.; Li, X.; Gao, X. Tartaric Acid Additive to Enhance Perovskite Multiple Preferential Orientations for High-Performance Solar Cells. *J. Energy Chem.* **2022**, *69*, 406−413.
(48) Popelier, P. L. A. Non-Covalent Interactions from a Quantum Chemical Topology Perspective. *J. Mol. Model.* **2022**, *28* (9), No. 276.
(49) Lu, T.; Chen, Q. Interaction Region Indicator: A Simple Real Space Function Clearly Revealing Both Chemical Bonds and Weak Interactions. *Chem.−Methods* **2021**, *1* (5), 231−239.
(50) Lefebvre, C.; Rubez, G.; Khartabil, H.; Boisson, J. C.; Contreras-García, J.; Hénon, E. Accurately Extracting the Signature of Intermolecular Interactions Present in the NCI Plot of the Reduced Density Gradient: Versus Electron Density. *Phys. Chem. Chem. Phys.* **2017**, *19* (27), 17928−17936.
(51) Bader, R. F. W.; Essén, H. The Characterization of Atomic Interactions. *J. Chem. Phys.* **1984**, *80* (5), 1943−1960.
(52) Cossard, A.; Casassa, S.; Gatti, C.; Desmarais, J. K.; Erba, A. Topology of the Electron Density and of Its Laplacian from Periodic Lcao Calculations on F-Electron Materials: The Case of Cesium Uranyl Chloride. *Molecules* **2021**, *26* (14), No. 4227.
(53) Iribarren, I.; Sánchez-Sanz, G.; Alkorta, I.; Elguero, J.; Trujillo, C. Evaluation of Electron Density Shifts in Noncovalent Interactions. *J. Phys. Chem. A* **2021**, *125* (22), 4741−4749.
(54) Afroz, M. A.; Gupta, R. K.; Garai, R.; Hossain, M.; Tripathi, S. P.; Iyer, P. K. Crystallization and Grain Growth Regulation through Lewis Acid-Base Adduct Formation in Hot Cast Perovskite-Based Solar Cells. *Org. Electron.* **2019**, *74*, 172−178.
(55) Huang, J.; Tan, S.; Lund, P. D.; Zhou, H. Impact of H2O on Organic-Inorganic Hybrid Perovskite Solar Cells. *Energy Environ. Sci.* **2017**, *10* (11), 2284−2311.
(56) Jong, U. G.; Yu, C. J.; Ri, G. C.; McMahon, A. P.; Harrison, N. M.; Barnes, P. R. F.; Walsh, A. Influence of Water Intercalation and Hydration on Chemical Decomposition and Ion Transport in Methylammonium Lead Halide Perovskites. *J. Mater. Chem. A* **2018**, *6* (3), 1067−1074.
(57) Xiao, L.; Xu, J.; Luan, J.; Zhang, B.; Tan, Z.; Yao, J.; Dai, S. Achieving Mixed Halide Perovskite via Halogen Exchange during Vapor-Assisted Solution Process for Efficient and Stable Perovskite Solar Cells. *Org. Electron.* **2017**, *50*, 33−42.
(58) Uyanga, K. A.; Ezike, S. C.; Onyedika, A. T.; Kareem, A. B.; Chiroma, T. M. Effect of Acetic Acid Concentration on Optical Properties of Lead Acetate Based Methylammonium Lead Iodide Perovskite Thin Film. *Opt. Mater.* **2020**, *109*, No. 110456.
(59) Heo, J. H.; Han, H. J.; Kim, D.; Ahn, T. K.; Im, S. H. Hysteresis-Less Inverted $CH_3NH_3PbI_3$ Planar Perovskite Hybrid Solar Cells with 18.1% Power Conversion Efficiency. *Energy Environ. Sci.* **2015**, *8* (5), 1602−1608.
(60) Miller, O. D.; Yablonovitch, E.; Kurtz, S. R. Strong Internal and External Luminescence as Solar Cells Approach the Shockley-Queisser Limit. *IEEE J. Photovoltaics* **2012**, *2* (3), 303−311.
(61) Luo, D.; Su, R.; Zhang, W.; Gong, Q.; Zhu, R. Minimizing Non-Radiative Recombination Losses in Perovskite Solar Cells. *Nat. Rev. Mater.* **2020**, *5*, 44−60.
(62) Mao, H.; Huang, Y.; Ma, Z.; Jin, L.; Tian, L.; Li, Y.; Yu, H.; Peng, C. Surface Grain Boundary Passivation via Mixed Antisolvent and PC 61 BM Assistant for Stable Perovskite Solar Cells. *J. Mater. Sci.: Mater. Electron.* **2019**, *30* (4), 3511−3520.
(63) Wang, Q.; Lin, F.; Chueh, C. C.; Zhao, T.; Eslamian, M.; Jen, A. K. Y. Enhancing Efficiency of Perovskite Solar Cells by Reducing Defects through Imidazolium Cation Incorporation. *Mater. Today Energy* **2018**, *7*, 161−168.
(64) Liu, M.; Johnston, M. B.; Snaith, H. J. Efficient Planar Heterojunction Perovskite Solar Cells by Vapour Deposition. *Nature* **2013**, *501* (7467), 395−398.
(65) Hu, Z.; An, Q.; Xiang, H.; Aigouy, L.; Sun, B.; Vaynzof, Y.; Chen, Z. Enhancing the Efficiency and Stability of Triple-Cation Perovskite Solar Cells by Eliminating Excess PbI_2 from the Perovskite/Hole Transport Layer Interface. *ACS Appl. Mater. Interfaces* **2020**, *12*, 54824−54832.
(66) Zheng, R.; Zhao, S.; Zhang, H.; Li, H.; Zhuang, J.; Liu, X.; Li, H.; Wang, H. Defect Passivation Grain Boundaries Using 3-Aminopropyltrimethoxysilane for Highly Efficient and Stable Perovskite Solar Cells. *Sol. Energy* **2021**, *224*, 472−479.
(67) Yang, I. S.; Park, N. G. Dual Additive for Simultaneous Improvement of Photovoltaic Performance and Stability of Perovskite Solar Cell. *Adv. Funct. Mater.* **2021**, *31* (20), No. 2100396.
(68) Kruszyńska, J.; Sadegh, F.; Patel, M. J.; Akman, E.; Yadav, P.; Tavakoli, M. M.; Gupta, S. K.; Gajjar, P. N.; Akin, S.; Prochowicz, D. Effect of 1,3-Disubstituted Urea Derivatives as Additives on the Efficiency and Stability of Perovskite Solar Cells. *ACS Appl. Energy Mater.* **2022**, *5* (11), 13617−13626.
(69) Wang, P.; Jiang, Q.; Zhao, Y.; Chen, Y.; Chu, Z.; Zhang, X.; Zhou, Y.; You, J. Synergistic Improvement of Perovskite Film Quality for Efficient Solar Cells via Multiple Chloride Salt Additives. *Sci. Bull.* **2018**, *63* (11), 726−731.
(70) Kang, Y.-J.; Na, S.-I. Multi-Site Passivation-Based Antisolvent Additive Engineering with Gradient Distribution for Superior Triple Cation P-I-N Perovskite Solar Cells. *Nano Energy* **2022**, *97*, No. 107193.
(71) Su, R.; Xu, Z.; Wu, J.; Luo, D.; Hu, Q.; Yang, W.; Yang, X.; Zhang, R.; Yu, H.; Russell, T. P.; Gong, Q.; Zhang, W.; Zhu, R. Dielectric Screening in Perovskite Photovoltaics. *Nat. Commun.* **2021**, *12* (1), No. 2479.

https://doi.org/10.1021/acsomega.3c07592
ACS Omega 2024, 9, 2674−2686

(72) Kim, D. I.; Lee, J. W.; Jeong, R. H.; Boo, J. H. A High-efficiency and Stable Perovskite Solar Cell Fabricated in Ambient Air Using a Polyaniline Passivation Layer. *Sci. Rep.* **2022**, *12*, No. 697.
(73) Zheng, H.; Liu, G.; Wu, W.; Xu, H.; Pan, X. Highly Efficient and Stable Perovskite Solar Cells with Strong Hydrophobic Barrier via Introducing Poly(Vinylidene Fluoride) Additive. *J. Energy Chem.* **2021**, *57*, 593−600.
(74) Kumar, P.; Jain, S. C.; Kumar, V.; Chand, S.; Tandon, R. P. Trap Filled Limit and High Current-Voltage Characteristics of Organic Diodes with Non-Zero Schottky Barrier. *J. Phys. D: Appl. Phys.* **2008**, *41* (15), No. 155108.
(75) Shariatinia, Z. Recent Progress in Development of Diverse Kinds of Hole Transport Materials for the Perovskite Solar Cells: A Review. *Renewable Sustainable Energy Rev.* **2020**, *119*, No. 109608.
(76) Pockett, A.; Eperon, G. E.; Sakai, N.; Snaith, H. J.; Peter, L. M.; Cameron, P. J. Microseconds, Milliseconds and Seconds: Deconvoluting the Dynamic Behaviour of Planar Perovskite Solar Cells. *Phys. Chem. Chem. Phys.* **2017**, *19* (8), 5959−5970.
(77) Pockett, A.; Eperon, G. E.; Peltola, T.; Snaith, H. J.; Walker, A.; Peter, L. M.; Cameron, P. J. Characterization of Planar Lead Halide Perovskite Solar Cells by Impedance Spectroscopy, Open-Circuit Photovoltage Decay, and Intensity-Modulated Photovoltage/Photocurrent Spectroscopy. *J. Phys. Chem. C* **2015**, *119* (7), 3456−3465.
(78) Caprioglio, P.; Wolff, C. M.; Sandberg, O. J.; Armin, A.; Rech, B.; Albrecht, S.; Neher, D.; Stolterfoht, M. On the Origin of the Ideality Factor in Perovskite Solar Cells. *Adv. Energy Mater.* **2020**, *10* (27), No. 2000502.
(79) Pham, N. D.; Tiing, V.; Yao, D.; Martens, W.; Guerrero, A.; Bisquert, J.; Wang, H. Guanidinium Thiocyanate Selective Ostwald Ripening Induced Large Grain for High Performance Perovskite Solar Cells. *Nano Energy* **2017**, *41*, 476−487.
(80) Choi, J.; Kamaraj, E.; Park, H.; Ho, B.; Won, H.; Park, S.; Joon, H. Dyes and Pigments Defect-Passivation of Organometal Trihalide Perovskite with Functionalized Organic Small Molecule for Enhanced Device Performance and Stability. *Dyes Pigm.* **2021**, *189*, No. 109255.
(81) Rad, R. R.; Ganji, B. A.; Taghavinia, N. 4-Tert-Butyl Pyridine Additive for Moisture-Resistant Wide Bandgap Perovskite Solar Cells. *Opt. Mater.* **2022**, *123*, No. 111876.
(82) Su, L.; Xiao, Y.; Han, G.; Lu, L.; Li, H.; Zhu, M. Performance Enhancement of Perovskite Solar Cells Using Trimesic Acid Additive in the Two-Step Solution Method. *J. Power Sources* **2019**, *426*, 11−15.

https://doi.org/10.1021/acsomega.3c07592
ACS Omega 2024, 9, 2674−2686